Li3V2(PO4)3 sintering atmosphere optimisation for its integration in all-solid-state batteries

Timothée Fabre, Marie Lachal, Hari Raj, Valérie Pralong, Renaud Bouchet, Marlu César Steil

Journal of the European Ceramic Society 45 (2025) 116941

Contents lists available at ScienceDirect

Journal of the European Ceramic Society

journal homepage: www.elsevier.com/locate/jeurceramsoc

$Li_3V_2(PO_4)_3$ sintering atmosphere optimisation for its integration in all-solid-state batteries

Timothée Fabre [a], Marie Lachal [a], Hari Raj [b], Valérie Pralong [b,c], Renaud Bouchet [a], Marlu César Steil [a,*]

[a] University Grenoble Alpes, Université Savoie Mont Blanc, CNRS, Grenoble INP, LEPMI, Grenoble 38000, France
[b] Normandie University, Ensicaen, Unicaen, CNRS, Crismat, Caen 14000, France
[c] Réseau sur le Stockage Electrochimique de l'Énergie (RS2E), Amiens 80039, France

ARTICLE INFO

Keywords:
Sintering
Atmosphere
LVP
Li-ion battery
ASSB

ABSTRACT

Integration of active materials into the architecture of all-solid-state batteries represents a significant scientific inquiry. $Li_3V_2(PO_4)_3$ (LVP), a positive and negative electrode active material for Li-ion batteries, has been subject to extensive research to elucidate its electrochemical behaviour during cycling processes. However, the comprehensive analysis of its thermal behaviour under different sintering atmosphere conditions has remained underexplored, particularly in the context of its compatibility with solid electrolytes. This study presents a meticulous study of sintering process under different atmospheres with precise control over oxygen partial pressure. Interestingly, we were able to sinter LVP and obtain dense, pure ceramic phase under slightly oxidising atmosphere, characterized by conductivity properties analogous to those observed in samples sintered under Ar/H_2 conditions. The findings of this investigation contribute to the understanding of the optimal conditions required for the sintering of LVP, paving the way for the co-sintering of this material with inorganic solid electrolyte unstable under reducing atmosphere, such as LATP.

1. Introduction

All-solid-state battery (ASB) technologies are the subject of intensive research, as they could pave the way for safer batteries without flammable liquid electrolyte, and increase energy density [1–3]. Especially, oxide-based solid electrolytes are very attractive in terms of ionic conductivity, electrochemical window, chemical and thermal stability [4]. However, one of the main drawbacks of such a system is the bad interface between the electrolyte and the active material, which leads to poor performances of the final system [5,6]. The ceramic processing is the key of this technology, in order to increase the compactness of the composite by sintering, forming intimate interface and grains boundaries, with no or limited reactivity between active material (AM) and electrolyte.

Two of the most studied oxide electrolytes are NASICON-type $Li_{1+x}Al_xTi_{2-x}(PO_4)_3$ (LATP) and garnet-type $Li_7La_3Zr_2O_{12}$ (LLZO). They have been co-sintered under air with a wide range of common AMs sensible to reduction: $LiCoO_2$ (LCO) [7–10] with sintering from 500°C to 700°C, $LiNi_xMn_yCo_{1-x-y}O_2$ (NMC) [11–16] with sintering from 400°C to 800°C, or high voltage spinels [17] with sintering from 400°C to 800°C. In all cases, the reactivity is too significant. Few studies explored co-sintering with different atmosphere like N_2 [16], argon [18] or argon + H_2 (Ar/H_2) [19] with the same AMs but degradation is still inevitable because of reduction of the phases and intrinsic chemical incompatibility. Another approach is to use phosphate-based AMs like $LiFePO_4$ (LFP) or $LiMnPO_4$ (LMP) which are sensible to reduction. They do react with LLZO by co-sintering in reductive atmosphere of Ar/H_2 [20,21] as phases are still chemically incompatible. LATP, being a phosphate-based phase, could be the only viable option with the appropriate atmosphere. Logically, co-sintering LATP with LFP under air leads to detrimental reactivity [22]. If LATP can be prone to reduction under Ar/H_2 [23], according to different studies, co-sintering in argon [18,24] or N_2 [25,26] is giving promising results with limited reactivity. Also, $Li_3V_2(PO_4)_3$ (LVP) phosphate phase compatibility with $Li_{1.5}Al_{0.5}Ge_{1.5}(PO_4)_3$ (LAGP) has been reported once, with co-sintering under argon leading to few impurities [27]. To this extent, LVP phase seems an interesting candidate.

For the past twenty years, LVP has raised a substantial interest as an

* Corresponding author.
E-mail address: cesar.steil@lepmi.grenoble-inp.fr (M.C. Steil).

https://doi.org/10.1016/j.jeurceramsoc.2024.116941
Received 11 July 2024; Received in revised form 16 September 2024; Accepted 20 September 2024
Available online 23 September 2024

electrode active material (AM), mostly as positive material for Li-ion batteries. It has been studied since the investigation of other polyanionic compounds like LFP [28]. One of its first synthesis has been done by Gaubicher et al. [29] by ionic exchange from the $Na_3V_2(PO_4)_3$ phase, giving NASICON rhombohedral phase. However, an easier direct synthesis by solid state route has been done by Sato et al. [30], obtaining an orthorhombic phase by high temperature heat treatment (1100°C) under argon. Eventually, Patoux et al. [31] showed that a monoclinic phase can be obtained by a direct aqueous route followed by an annealing at only 750°C under a gas flow of N_2/H_2 (10 %). Since when, research has mainly focused on new synthesis route of the material, like sol-gel method, hydrothermal method, or freeze-drying method [32]; improving its electronic conductivity thanks to carbon coating and ion doping [33], or nanostructuration [34,35].

LVP main interests are its low price and low toxicity, but also its good electrochemical performance thanks to its chemical and thermal stability due to the polyanionic structure. Its structural stability can be explained by the phosphate polyanionic backbone, consisting of "lantern" patterns composed of VO_6 octahedra and PO_4 tetrahedra. Because the vanadium can adopt different degrees of oxidation (V^{+III}/V^{+II}, V^{+IV}/V^{+III} and V^{+V}/V^{+IV}), the operated potential of the LVP can take a broad range of value from +1.5 to +4.5 V vs Li, leading eventually to complex extraction processes [36,37]. Nevertheless, very good stability in cycling has been confirmed by numerous studies with both reversible extraction up to 2 Li^+ (V^{+III} to V^{+IV}, 3.5 – 4.2 V vs Li) [38–41], as well as insertion of 2 Li^+ (V^{+III} to V^{+II}, 1.5–2 V vs Li), opening the path to using this material as an active material for negative electrodes [31,42] and realising symmetrical LVP (-)/LVP (+) systems.

Few studies used LVP in monolithic ASB systems. Kobayashi et al. [43,44] used screen printing of composite electrodes on a pellet of $Li_{1.5}A_{0.5}Ge_{1.5}(PO_4)_3$ (LAGP) electrolyte with LVP followed by hot pressing to obtain a symmetric solid-state system. Bouchet et al. [45,46] used Spark Plasma Sintering (SPS) to obtain monolithic symmetric systems, also with LAGP electrolyte. Finally, Yu et al. [47] as well used screen printing of the electrode on LATP electrolyte. Yet, the temperature-dependent behaviour of LVP has not been studied to date. The nature of the atmosphere, e.g., reducing, "neutral" or oxidising, is a fundamental parameter for phase temperature stability. For example, LATP is known to be synthesized and stable under air, while LVP is synthesized and stable under Ar/H_2. With this in mind, we recently published a study on the optimization of LATP sintering under argon [48].

Herein, we present an extensive study of the sintering behaviour of monoclinic LVP powders as function of partial pressure of oxygen by dilatometric analysis, microstructural and structural investigations (thanks to scanning electron microscopy and X-ray diffraction, respectively). In addition, the electrical conductivity of the LVP pellets were characterized by electrochemical impedance spectroscopy.

2. Experimental

2.1. Sample processing

- **Synthesis of $Li_3V_2(PO_4)_3$**

  $Li_3V_2(PO_4)$ (LVP) monoclinic phase was synthesized by direct ceramic synthesis. Lithium carbonate (Li_2CO_3), vanadium oxide (V_2O_5) and $NH_4H_2PO_4$ precursors were ground in mortar pestle for 2 h and first pre-calcined at 350°C for 5 h in an alumina crucible under argon + 10 % H_2 atmosphere to remove gases compounds. The pre-calcined precursors were again ground in mortar pestle for 30 min before calcination at 850°C for 12 h under argon + 10 % H_2 atmosphere. The final crystalline powder of LVP was further ground for 30 min before XRD analysis.
- **Ball milling and pellets shaping**

Pristine LVP powder was grounded by planetary ball milling (Pulverisette 7 classic line, Fristch) at 400 rpm for 1 h in a zirconia bowl with balls of diameter 5 mm. Particle size distribution was controlled with a Malvern Mastersizer 3000 laser granulometer. Pristine LVP and ball milled BM-LVP powders were compacted first with a uniaxial press under 40 MPa in a die of 8 mm in diameter, then with an isostatic press under 250 MPa. Green compacts with a relative density of 65 % TD (theoretical density of monoclinic $Li_3V_2(PO_4)_3 = 3.03\ g.cm^{-3}$) [49] were obtained. The green compacts were measured around 8 mm in diameter (~ 0.45 cm^2 in area) and between 2 and 3 mm in thickness after isostatic compaction.

2.2. Sintering

Evolution of the linear shrinkage in temperature was followed with a dilatometer DIL 402 C from Netzsch, up to 1100°C at 5 °C/min under different oxygen partial pressure (pO_2) using dry air, argon flux (8 L/h) with controlled pO_2 (10^{-3} atm, 3.10^{-4} atm and 3.10^{-5} atm), and finally argon + 3 % H_2 flux at 8 L/h (Ar/H_2). The pO_2 was controlled thanks to oxygen pump and gauge system [50]. Conventional Sintering (CS) was also performed at temperature from 800°C to 1020°C for 1 h at 5 °C/min under argon flux (8 L/h, $pO_2 = 5.10^{-6}$ atm) and argon + 3 % H_2 flux at 8 L/h (Ar/H_2). The green pellets were placed in alumina crucible in a powder covering bed. The apparent density of the sintered pellets was obtained by Archimedes' method in ethanol at room temperature.

2.3. Sample characterization

The sample structure and purity (powders before and after ball milling, as well as green samples and pellet after CS were analysed by X-ray diffraction (XRD). Data were collected from a PANalytical X'Pert Pro MPD diffractometer using θ/2θ Bragg-Brentano geometry with a Cu-K_α radiation (1.5406 Å).

The microstructure was examined using a Field Emission Gun SEM (Zeiss Ultra 55) on powders and cross sections of the pellets after CS. SEM images were performed with secondary electrons at magnitude × 500, × 1k and × 10k.

The electrical conductivity was determined by impedance spectroscopy on the sintered pellets with a VMP-300 from Biologic on a range of temperatures from −20°C to 110°C. A thin gold layer of around 500 nm was deposited by PVD on the pellet surfaces to optimise electrical contacts prior to impedance measurements. The excitation signal was set from 20 mV to 400 mV depending on the temperature and the impedance of the samples with frequencies varying from 10^7 Hz to 500 mHz. The conductivity was determined from the Nyquist plots and the geometrical factor of the pellet. Measurements were recorded with EC-Lab software and data (Nyquist diagrams) were analysed and fitted with Zview software (Scribner Associates Incorporated).

3. Results and discussion

3.1. Powder morphology and sintering

Fig. 1a displays the volumetric distribution of the particle size for LVP and BM-LVP powders and demonstrates that the planetary ball milling has a strong impact on the particle size distribution.

It allows to reduce the mean particle diameter in volume ($D_{v,50}$) 33 times from 60.4 μm to 1.8 μm. In addition, a narrower volumetric distribution is obtained for the BM-LVP powder. The corresponding morphology is presented on SEM images on Fig. 2b and (c). LVP powder is composed of agglomerates with a large size distribution from few micrometres to few 100 of micrometres in concordance with the granulometric distribution, and made up of sintered primary particles (1–2 μm). The agglomerates are crushed in smaller particles (1–2 μm) during ball milling, though few small agglomerates still remain ass show in Fig. 2c. X-ray diffraction (XRD) patterns of LVP and BM-LVP powder recorded at room temperature are given in Fig. 2a. There is no noticeable

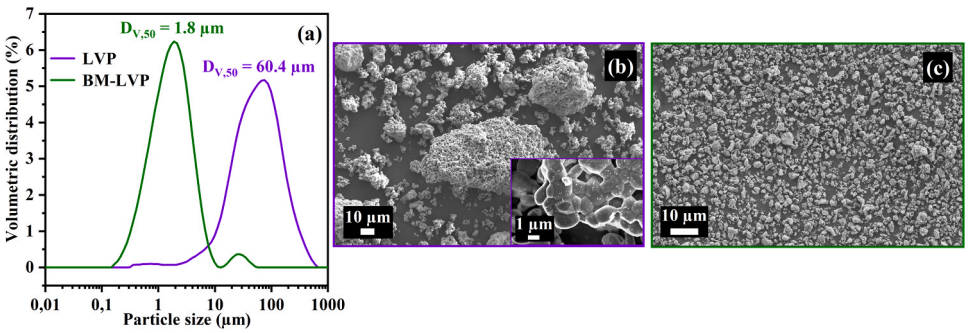

Fig. 1. (a) Volumetric particle size distribution of LVP (purple) and BM-LVP (green) powders; corresponding SEM images at (b) magnification of × 500 and × 10k (insert) for LVP, (c) × 1k for BM-LVP.

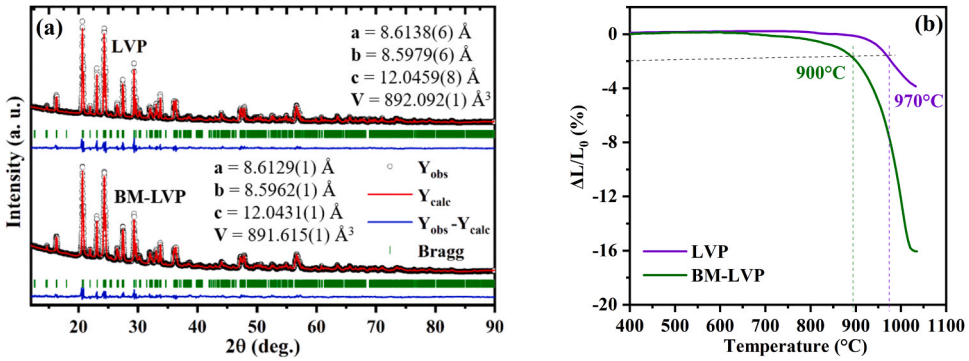

Fig. 2. (a) Rietveld refinement pattern of LVP and BM-LBP powders. In the refinement graphs, experimental, calculated, difference plots are shown by red, black and blue colors, respectively, whereas, Bragg diffraction peaks are shown by vertical green lines; (b) Dilatometry curves (linear shrinkage versus temperature) for LVP (purple) and BM-LVP (green) under Ar/H_2 with corresponding derivative in dashed line.

change found in the XRD peaks of LVP before and after ball milling. The XRD of LVP and BM-LVP match with PDF #96–412–4524 of $Li_3V_2(PO_4)_3$ having monoclinic structure of space group $P2_1/c$. For more structural information and determining crystal lattice parameters, Rietveld refinements are performed on the XRD patterns of LVP and BM-LVP powder samples using FullProf Suite. In both cases, the monoclinic remains unchanged, thus the ball milling did not damage the crystallographic structure.

Conventional sintering was carried out by dilatometry under Ar/H_2 on LVP and BM-LVP to analyse the granulometry effect on the densification. The evolution of the linear shrinkage as function of the temperature is observed on Fig. 2b. The starting sintering temperature was arbitrary chosen at −2 % of the linear shrinkage $\Delta L/L_0$. Reducing the $D_{v,50}$ from 60 to approx. 2 µm (Fig. 1a) enables to noticeably lower the starting sintering temperature from 970 ± 5°C to 900 ± 5°C (Fig. 2b) and the linear shrinkage $\Delta L/L_0$ considerably decreases from −6.3 % to −16.1 %. Experiments were stopped at 1030°C in order to avoid the monoclinic phase $Li_3V_2(PO_4)_3$ compounds to evolve into the orthorhombic phase at higher temperatures [31].

To conclude, to densify LVP powder under Ar/H2 at a temperature

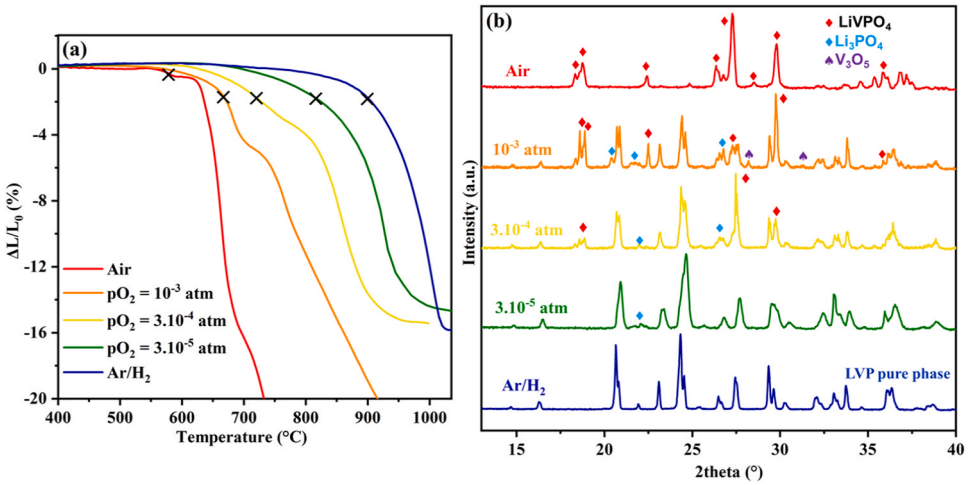

Fig. 3. (a) Shrinkage curves of BM-LVP sintered under air (red), argon with different pO_2 (10^{-3} atm, 3.10^{-4} atm and 3.10^{-5} atm) and under Ar/H_2 (blue) with cross indicating beginning of sintering (b) XRD patterns of the samples after dilatometric analysis at different atmospheres; Ar/H_2 pure phase pellet used as reference being equivalent to LVP powder (Fig. 2).

lower than its phase change (i.e. 1030°C), the average grain size must be reduced to less than 2 μm. For the next part, all the sintering processes are performed on BM-LVP.

3.2. $Li_3V_2(PO_4)_3$ sintering: atmosphere effect

BM-LVP was sintered in dilatometer under different O_2 partial pressure: air, argon at pO_2 of 10^{-3} atm, 3.10^{-4} atm and 3.10^{-5} atm, and argon + 3 % H_2 (Ar/H_2). Powder shrinkage versus temperature curves obtained under different atmospheres (Fig. 3a) of BM-LVP show significant variations in sintering behaviour as a function of oxygen partial pressure (pO_2). The XRD diagrams obtained for the different pellets after dilatometer testing are shown in Fig. 3b. They highlight structural changes as a function of sintering atmosphere.

First of all, the sintering was carried out under air. As shown in Fig. 3a (red curve), a slight shrinkage step can be seen at around 580°C, before melting of the phase at higher temperature. Patoux *et al.* found that LVP is not stable in air at higher temperature than 530°C [31], with V^{+III} oxidising to V^{+IV}, which could relate to this first step. As shown in Fig. 3b, The XRD pattern of the melted pellet displays total phase change in oxidised $LiVOPO_4$ phase, with V^{+IV}. This is consistent with studies showing that LVP converts in $LiVOPO_4$ under air between 600°C and 700°C [51,52]. It has also been reported that heating $LiVOPO_4$ under air at a temperature higher than 700°C result in melting of the phase [53], consistent with our findings on LVP sample sintered in air.

The shrinkage curves obtained for different pO_2 values show an increase in the temperature at which sintering begins as pO_2 decreases (Fig. 3a). Interestingly, for values of 1.10^{-3} atm and 3.10^{-4} atm, the samples show intermediate behaviour between melting and sintering. At 1.10^{-3} atm, the material starts sintering at 670°C and then, after a decrease in shrinkage rate at 750°C, melts. For 3.10^{-4} atm, the material starts sintering at 750°C, then after a decrease in shrinkage rate, shrinkage continues until it stabilizes at around 950°C, indicating the end of densification without melting. The XRD diagrams of samples heat-treated at 1.10^{-3} atm and 3.10^{-4} atm show a significant structural change, with the appearance of the Li_3PO_4, V_3O_5 and $LiVOPO_4$ phases (Fig. 3b). This change in sintering temperature can be explained by an initial change in the LVP phase to $LiVOPO_4$ caused by an excessively oxidising atmosphere, with this phase beginning to melt at 700°C. The appearance of a liquid phase improves mass transport and therefore sintering kinetics.

However, there is a competition with reactivity: if the atmosphere is too oxidising, here at a pO_2 of 1.10^{-3} atm, the pellet does not densify and melts completely. At 3.10^{-4} atm, the $LiVOPO_4$ phase appears but in a smaller proportion, so the sintering temperature rises slightly and the pellet can finally densify before melting. With a pO_2 of 3.10^{-5} atm, sintering starts at around 810 ± 5°C (Fig. 3a, green curve), whereas it begins at 900 ± 5°C (Fig. 3a, blue curve) under Ar/H_2 for the same powder. The DRX diagram of the sample treated at 3.10^{-5} atm, compared with that of the sample treated under Ar/H_2, shows slight modifications linked to weak LVP oxidation not leading to the formation of $LiVOPO_4$-type impurities. This shows that LVP can be sintered in a slightly oxidising atmosphere up to this partial oxygen pressure.

To clarify this point, a series of samples were sintered under argon flux in a controlled atmosphere furnace, with the partial pressure of oxygen measured with a gauge and set at a value of 5.10^{-6} atm. The following conditions were chosen: plateau temperatures (950, 980, 1000 and 1020°C) for 1 h with a powder bed, and covered with powder. A point of comparison was carried out under Ar/H_2 for 1 h at 1000°C, the results being summarised in Table 1. Under argon, the maximum relative density reached 97.8 ± 0.1 % at 950°C. Thereafter, a slight decrease in density is observed for pellets sintered at temperatures above 950°C. The pellet sintered under Ar/H_2 at 1000°C has a density of 97.1 ± 0.1 %, similar to that obtained under argon at 950°C.

Fig. 4 displays the microstructures of fractured surfaces of pellets sintered at 950°C and 1000°C under argon ($pO_2 = 5.10^{-6}$ atm), and at 1000°C under Ar/H_2 as a reference. At 950°C (Fig. 4a), a fully dense pellet is obtained (d = 97.8 ± 0.1 %). It can be noted that the grain size increases with the sintering temperature under argon and it seems that it is smaller after the sintering at 1000°C under argon than under Ar/H2 (Fig. 4(b) et 4(c)). The grain size is homogeneous and can reach 2–5 μm.

Table 1
Density measured by Archimedes' method for BM-LVP pellets sintered at various temperatures under argon ($pO_2 = 5.10^{-6}$ atm) and at 1000°C under Ar/H_2 (relative density of green samples is 65 %).

Sintering temperature	950°C	980°C	1000°C	1020°C
Density ± 0.1 % (argon, $pO_2 = 5.10^{-6}$ atm)	97.8 %	96.7 %	94.9 %	94.0 %
Density ± 0.1 % (Ar/H_2)	×	×	97.1 %	×

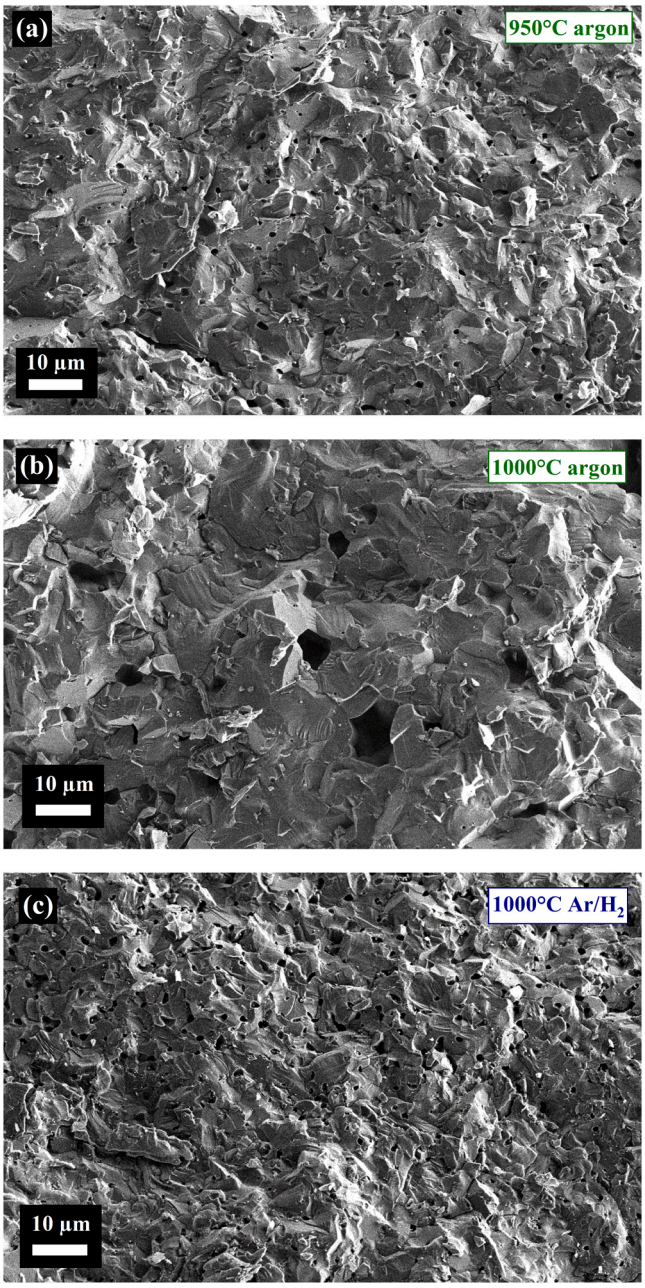

Fig. 4. SEM images of BM-LVP pellets fractures at magnification of × 1k after sintering under argon ($pO_2 = 5.10^{-6}$ atm) at (a) 950°C and (b) 1000°C; (c) under Ar/H_2 at 1000°C.

A small close residual porosity is observed with pores diameters below 1 μm. At 1000°C (Fig. 4b), significant large pores appear, comprising regular pores of diameter in between 10 and 20 μm. This porosity may be due to gas release and structural changes in the LVP at temperatures above 950°C, as will be discussed in the following with the analysis of Fig. 5. Accordingly, the density decreased to 94.0 ± 0.1 %. Under Ar/H_2, fractured pellet (Fig. 4c) displays a dense and homogenous microstructure similar to the one of BM-LVP fully sintered at 950°C under argon. The measured density of 97.1 ± 0.1 % is consistent with these observations.

The XRD patterns of pellets sintered under argon ($pO_2 = 5.10^{-6}$ atm) at different temperatures are shown in Fig. 5a. The diffractograms show little change as a function of temperature up to 1020°C, when a change in peak intensity at 29.6° is noticeable. A closer comparison between argon sintering at 950°C (green), 1000°C (orange) and Ar/H_2 sintering at 1000°C (blue) is shown in Fig. 5b. Under argon atmosphere, at 950°C, we can see the beginning of a modification with the presence of a Li_3PO_4 impurity, with peaks appearing at 22.4° and 24.7°. At 1000°C, this impurity is still present, along with a second additional impurity V_3O_5 with peaks at 27° and 31.2°. These impurities can be correlated with the large pores observed in the microstructure of the sample sintered at 1000°C under argon in Fig. 4e.

In Fig. 6, the purity of the pellet sintered under Ar/H_2 at 1000°C is confirmed by Rietveld refinement, with practically no difference from the PDF #96–412–4524 corresponding to the $Li_3V_2(PO_4)_3$ monoclinic phase. Moreover, the sample sintered under argon ($pO_2 = 5.10^{-6}$ atm) at 950°C can also be perfectly refined with the same PDF. Structural differences are almost undetected by this method. The onset of phase oxidation at 950°C, reflected by the appearance of the Li_3PO_4 impurity, does not lead to any structural change in the material.

Hence, it is demonstrated here that phase pure and fully dense LVP pellet can be obtained by conventional sintering under argon with pO_2 of 5.10^{-6} atm at 950°C. This optimal densification allows to then compare the effect of sintering atmosphere on electrical properties, between the sample sintered at 950°C under argon and the sample sintered at 1000°C under Ar/H_2.

3.3. Electrical Conductivity

Electrochemical impedance spectroscopy has been used to determine the conductivity of the different samples depending on the sintering atmosphere. The impedance spectra measured at 100°C are shown in Fig. 7a. It can be observed that a very similar behaviour is obtained for both sintering conditions, 950°C under argon ($pO_2 = 5.10^{-6}$ atm) and 1000°C under Ar/H_2, with a main contribution at high-frequencies (HF)

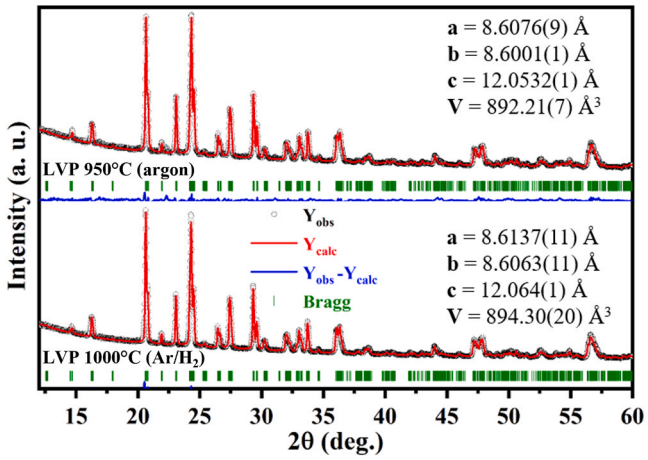

Fig. 6. Rietveld refinement of LVP pellets sintered at 950°C under argon ($pO_2 = 5.10^{-6}$ atm) and at 1000°C under Ar/H_2. In the refinement graphs, experimental, calculated and difference plots are represented by red, black and blue colors, respectively, while Bragg diffraction peaks are represented by green vertical lines.

between 7 MHz and 50 kHz, attributed to the bulk of LVP, followed by a small loop at mid-frequencies (MF) from 50 kHz to 1 kHz. In addition, capacitive behaviour below 400 Hz is a characteristic signature of a blocking gold electrode/LVP interface, indicating the predominantly ionic nature of this electrical conductivity. The discontinuity of the first semicircle at high frequency is due to a change of impedance meter current measurement range to a frequency of approx. 500 kHz.

The impedance diagrams can be fitted using an equivalent electrical circuit illustrated in Fig. 7a to extract the resistive and capacitive components of each semicircle. The resistances R_1 and R_2 are associated with the diameters of the high-frequency and mid-frequency semicircles respectively, and the capacitance associated with the process can be calculated from the CPE parameters. The effective capacitances determined for the HF semicircle in the measured temperature range are around 2.10^{-11} F/cm. This capacity value means that the HF semicircle corresponds to the intra-granular properties of the ceramic, i.e. the bulk properties of the LVP material [54]. In this case, bulk conductivity of LVP can be calculated from the bulk resistance of the samples to compare the intrinsic behaviour of the material.

The semicircle at mid-frequencies corresponds to a blocking effect at the internal interfaces between grains, often referred to as the grain boundaries (GB) contribution, with a capacitance of the order of 5.10^{-9}

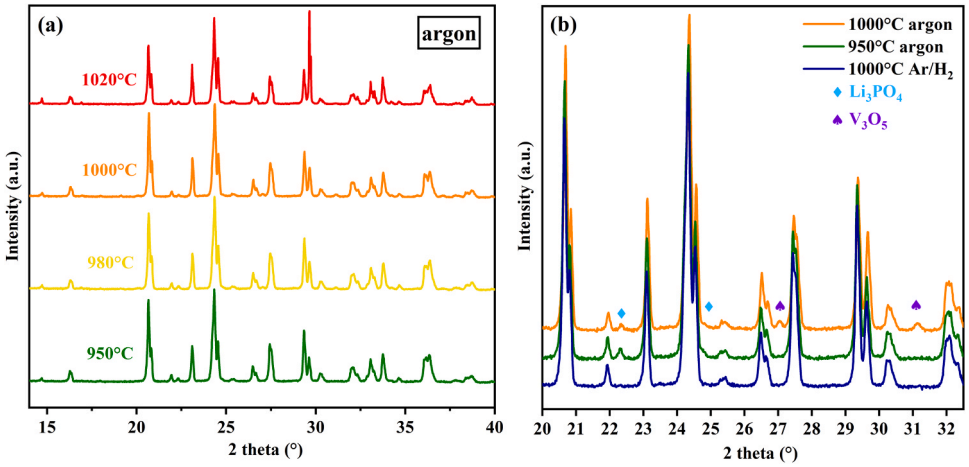

Fig. 5. Diffractograms of BM-LVP pellets (a) after sintering under argon ($pO_2 = 5.10^{-6}$ atm) at 950°C, 980°C, 1000°C and 1020°C; (b) Comparison between 20° and 32.5° of samples sintered under argon ($pO_2 = 5.10^{-6}$ atm) at 950°C and 1000°C with the reference sample sintered at 1000°C under Ar/H_2.

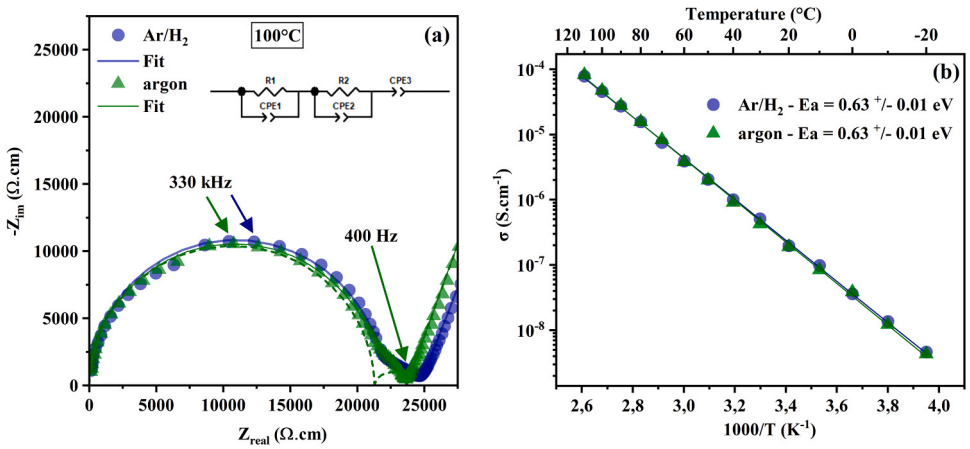

Fig. 7. (a) Nyquist plot at 100°C of LVP sintered pellets under argon ($pO_2 = 5.10^{-6}$ atm) in green at 950°C or under Ar/H_2 in blue at 1000°C (b) Bulk conductivity of the same samples between −20°C and 110°C.

F/cm. This effect is correlated with the microstructure of the sample [55]. Resistance and capacitance values calculated at 100°C are summarised in Table 2.

The bulk conductivities of the samples measured at different temperatures between −20°C and 110°C are plotted in Fig. 7b in Arrhenius coordinates. The two sets of data are almost over-imposed, which demonstrates the very good stability of the $Li_3V_2(PO_4)_3$ phase under argon compared with the reference sample sintered under Ar/H_2. The data obeys an Arrhenius behaviour with an activation energy E_a of 0.63 $^{+}$/- 0.01 eV for both samples sintered under Ar/H_2 and under argon. The bulk conductivity of phase pure LVP under argon is 1.90×10^{-7} S/cm at 20°C. By adding the GB contribution, the total conductivity is 1.60×10^{-7} S/cm. Details of bulk and total conductivities at 20°C for both samples are given in Table 3.

To our knowledge, only one study has determined the conductivity of a densified LVP pellet, but with the orthorhombic phase obtained at high temperature (1100°C), where it is concluded that conductivity is mainly ionic[30]. However, the vast majority of studies have focused on the monoclinic LVP phase, which offers better electrochemical properties. A few studies have determined the conductivity of monoclinic LVP by impedance spectroscopy, but only with powder tablets and not with sintered pellets [40,56,57]. In this respect, a conductivity value published in the work of S.-C. Yin *et al.* [56] of 2.4×10^{-7} S/cm, measured at 27°C and associated with electronic conduction, is widely used in the literature [35]. We believe that this value has been erroneously attributed to electronic conduction in the impedance diagram at the intersection of a high-frequency pseudo semicircle with the Z_{real} axis. This contribution would in fact correspond mainly to the bulk ionic properties of the material and is in agreement with the measurements obtained in this study.

4. Conclusion

This paper extensively studied the behaviour of LVP material in temperature depending on the atmosphere. First, we showed that thanks to particle size optimisation to lower than 2 μm by ball milling, it is possible to obtain full densification under Ar/H_2.

With to a precise control of the O_2 partial pressure of sintering atmosphere, the structural and microstructural properties of the sintered pellets shows that $Li_3V_2(PO_4)_3$ is stable in temperature up to 950°C under argon ($pO_2 = 5.10^{-6}$ atm) and 1000°C under Ar/H_2. At higher temperature than 950°C, a reactivity altering the microstructure starts to occur under argon. In this case, the sintering is completed, the microstructure is homogenous with a limited grain growth and the structural monoclinic phase is preserved but with the presence of Li_3PO_4 and V_3O_5 impurities. At increased temperatures, the reactivity is promoted creating porosity and thus lowering the overall relative density.

Our study allows to properly extract the electrical bulk conductivity of LVP, which appears to be mainly ionic at RT with a bulk conductivity value of 1.90×10^{-7} S/cm and E_a of 0.63 eV.

These results highlight the possibility to find a co-sintering window between active materials and inorganic electrolytes through precise particle size control, and careful choice for sintering temperature and atmosphere.

Table 2
Electrical properties measured at 100°C of samples sintered under argon at 950°C ($pO_2 = 5.10^{-6}$ atm) or under Ar/H_2 at 1000°C.

Samples	Bulk		Grain boundaries	
	R_1 (kΩ. cm)	C_1 (F/cm)	R_2 (kΩ. cm)	C_2 (F/cm)
950°C under argon ($pO_2 = 5.10^{-6}$ atm)	21.2	2.0×10^{-11}	2.4	4.2×10^{-9}
1000°C under Ar/H_2	21.5	1.9×10^{-11}	3.3	6.9×10^{-9}

Table 3
Bulk and total conductivities obtained at 20°C for the two samples.

Samples	σ_{bulk} (S/cm)	σ_{tot} (S/cm)
950°C under argon ($pO_2 = 5.10^{-6}$ atm)	1.9×10^{-7}	1.6×10^{-7}
1000°C under Ar/H_2	2.0×10^{-7}	1.7×10^{-7}

CRediT authorship contribution statement

Marlu Cesar Steil: Writing – review & editing, Supervision, Methodology, Funding acquisition. **Timothée Fabre:** Writing – original draft, Methodology, Investigation. **Marie Lachal:** Writing – original draft, Methodology, Investigation, Data curation. **Hari Raj:** Writing – review & editing, Investigation. **Valérie Pralong:** Writing – review & editing, Supervision, Resources. **Renaud Bouchet:** Writing – review & editing, Supervision, Resources, Project administration.

Declaration of Competing Interest

The authors declare that they have no known competing financial interests or personal relationships that could have appeared to influence the work reported in this paper.

Acknowledgements

This work was supported by the French National Research Agency through through the project Flashbat contract no. ANR-20-CE05–0040–02, by Institut Carnot Energies du Futur and by the Centre of Excellence of Multifunctional Architectured Materials "CEMAM".

References

[1] J. Janek, W.G. Zeier, A solid future for battery development, Nat. Energy 1 (2016) 16141.
[2] C. Sun, J. Liu, Y. Gong, D.P. Wilkinson, J. Zhang, Recent advances in all-solid-state rechargeable lithium batteries, Nano Energy 33 (2017) 363–386.
[3] S. Randau, et al., Benchmarking the performance of all-solid-state lithium batteries, Nat. Energy 5 (2020) 259–270.
[4] F. Zheng, M. Kotobuki, S. Song, M.O. Lai, L. Lu, Review on solid electrolytes for all-solid-state lithium-ion batteries, J. Power Sources 389 (2018) 198–213.
[5] A. Banerjee, X. Wang, C. Fang, E.A. Wu, Y.S. Meng, Interfaces and interphases in all-solid-state batteries with inorganic solid electrolytes, Chem. Rev. 120 (2020) 6878–6933.
[6] Y. Xiao, et al., Understanding interface stability in solid-state batteries, Nat. Rev. Mater. 5 (2020) 105–126.
[7] K. Park, et al., Electrochemical Nature of the Cathode Interface for a Solid-State Lithium-Ion Battery: interface between $LiCoO_2$ and Garnet-$Li_7La_3Zr_2O_{12}$, Chem. Mater. 28 (2016) 8051–8059.
[8] M. Ihrig, et al., Study of $LiCoO_2$/$Li_7La_3Zr_2O_{12}$:Ta interface degradation in all-solid-state lithium batteries, ACS Appl. Mater. Interfaces 14 (2022) 11288–11299.
[9] W.S. Scheld, et al., The riddle of dark LLZO: cobalt diffusion in garnet separators of solid-state lithium batteries, Adv. Funct. Mater. 33 (2023) 2302939.
[10] F. Ichihara, S. Miyoshi, T. Masuda, Co-sintering process of $LiCoO_2$ cathodes and NASICON-type LATP solid electrolytes studied by X-ray diffraction and X-ray absorption near edge structure. Phys. Chem. Chem. Phys. 24 (2022) 25878–25884.
[11] T. Demuth, et al., Influence of the sintering temperature on LLZO-NCM cathode composites for solid-state batteries studied by transmission electron microscopy, Matter 6 (2023) 2324–2339.
[12] T. Kato, et al., Effects of sintering temperature on interfacial structure and interfacial resistance for all-solid-state rechargeable lithium batteries, J. Power Sources 325 (2016) 584–590.
[13] J.P. Beaupain, et al., Reaction of $Li_{1.3}Al_{0.3}Ti_{1.7}(PO_4)_3$ and $LiNi_{0.6}Co_{0.2}Mn_{0.2}O_2$ in Co-sintered composite cathodes for solid-state batteries, ACS Appl. Mater. Interfaces 13 (2021) 47488–47498.
[14] M. Malaki, et al., Advanced analytical characterization of interface degradation in Ni-Rich NCM cathode co-sintered with LATP solid electrolyte, ACS Appl. Energy Mater. 5 (2022) 4651–4663.
[15] Y. Chen, et al., Insight into the extreme side reaction between $LiNi_{0.5}Co_{0.2}Mn_{0.3}O_2$ and $Li_{1.3}Al_{0.3}Ti_{1.7}(PO_4)_3$ during cosintering for all-solid-state batteries, Chem. Mater. 35 (2023) 9647–9656.
[16] S. Valiyaveettil-SobhanRaj, et al., High-temperature thermal reactivity and interface evolution of the NMC-LATP-carbon composite cathode, ACS Appl. Mater. Interfaces 15 (2023) 13689–13699.
[17] L. Miara, et al., About the compatibility between high voltage spinel cathode materials and solid oxide electrolytes as a function of temperature, ACS Appl. Mater. Interfaces 8 (2016) 26842–26850.
[18] M. Rumpel, et al., Thermal stabilities of Mn-based active materials in combination with the ceramic electrolyte LATP for ASSB bulk cathodes, Mater. Adv. 3 (2022) 4015–4025.
[19] S. Uhlenbruck, et al., Cathode-electrolyte material interactions during manufacturing of inorganic solid-state lithium batteries, J. Electroceram. 38 (2017) 197–206.
[20] Y. Ren, T. Liu, Y. Shen, Y. Lin, C.-W. Nan, Chemical compatibility between garnet-like solid state electrolyte $Li_{6.75}La_3Zr_{1.75}Ta_{0.25}O_{12}$ and major commercial lithium battery cathode materials, J. Mater. 2 (2016) 256–264.
[21] J. Wakasugi, H. Munakata, K. Kanamura, Thermal stability of various cathode materials against $Li_{6.25}Al_{0.25}La_3Zr_2O_{12}$ electrolyte, Electrochemistry 85 (2017) 77–81.
[22] C.-Y. Yu, J. Choi, V. Anandan, J.-H. Kim, High-temperature chemical stability of $Li_{1.4}Al_{0.4}Ti_{1.6}(PO_4)_3$ solid electrolyte with various cathode materials for solid-state batteries, J. Phys. Chem. C. 124 (2020) 14963–14971.
[23] M. Gellert, E. Dashjav, D. Grüner, Q. Ma, F. Tietz, Compatibility study of oxide and olivine cathode materials with lithium aluminum titanium phosphate, Ionics 24 (2018) 1001–1006.
[24] Q. Xu, et al., Active interphase enables stable performance for an all-phosphate-based composite cathode in an all-solid-state battery, Small 18 (2022) 2200266.
[25] M. Malaki, et al., Probing the Interface Evolution in Co-sintered All-Phosphate Cathode-Solid Electrolyte Composites, Adv. Mater. Interfaces (2023) 2300513.
[26] J.P. Beaupain, et al., Co-Sintering of $Li1_{1.3}Al_{0.3}Ti_{1.7}(PO_4)_3$ and $LiFePO_4$ in tape-casted composite cathodes for oxide solid-state batteries, Batteries 9 (2023) 543.
[27] Y. Liu, J. Chen, J. Gao, Preparation and chemical compatibility of lithium aluminum germanium phosphate solid electrolyte, Solid State Ion. 318 (2018) 27–34.
[28] K. Nanjundaswamy, Synthesis, redox potential evaluation and electrochemical characteristics of NASICON-related-3D framework compounds, Solid State Ion. 92 (1996) 1–10.
[29] J. Gaubicher, C. Wurm, G. Goward, C. Masquelier, L. Nazar, Rhombohedral form of $Li_3V_2(PO_4)_3$ as a cathode in Li-ion batteries, Chem. Mater. 12 (2000) 3240–3242.
[30] M. Sato, et al., Enhancement of discharge capacity of $Li_3V_2(PO_4)_3$ by stabilizing the orthorhombic phase at room temperature, Solid State Ion. 135 (2000) 137–142.
[31] S. Patoux, C. Wurm, M. Morcrette, G. Rousse, C. Masquelier, A comparative structural and electrochemical study of monoclinic $Li_3Fe_2(PO_4)_3$ and $Li_3V_2(PO_4)_3$, J. Power Sources 119 (121) (2003) 278–284.
[32] Y. Wang, X. Zhang, W. He, C. Wei, Q. Cheng, A review for the synthesis methods of lithium vanadium phosphate cathode materials, J. Mater. Sci.: Mater. Electron. 28 (2017) 18269–18295.
[33] C. Liu, R. Massé, X. Nan, G. Cao, A promising cathode for Li-ion batteries: $Li_3V_2(PO_4)_3$, Energy Storage Mater. 4 (2016) 15–58.
[34] H. Huang, S.-C. Yin, T. Kerr, N. Taylor, L.F. Nazar, Nanostructured composites: a high capacity, fast rate $Li_3V_2(PO_4)_3$/carbon cathode for rechargeable lithium batteries, Adv. Mater. 14 (2002) 1525–1528.
[35] H. Tan, et al., Nanostructured $Li_3V_2(PO_4)_3$ cathodes, Small 14 (2018) 1800567.
[36] W. Oh, H. Park, B.-S. Jin, R. Thangavel, W.-S. Yoon, Understanding the structural phase transitions in lithium vanadium phosphate cathodes for lithium-ion batteries, J. Mater. Chem. A 8 (2020) 10331–10336.
[37] T. Ruan, S. Lu, J. Lu, J. Niu, R. Li, Unraveling the intercalation chemistry of multi-electron reaction for polyanionic cathode $Li_3V_2(PO_4)_3$, Energy Storage Mater. 55 (2023) 546–555.
[38] M. Morcrette, J.-B. Leriche, S. Patoux, C. Wurm, C. Masquelier, In Situ x-ray diffraction during lithium extraction from rhombohedral and monoclinic $Li_3V_2(PO_4)_3$, Electrochem. Solid-State Lett. 6 (2003) A80–A84.
[39] M.Y. Saïdi, J. Barker, H. Huang, J.L. Swoyer, G. Adamson, Performance characteristics of lithium vanadium phosphate as a cathode material for lithium-ion batteries, J. Power Sources 119–121 (2003) 266–272.
[40] S.-C. Yin, H. Grondey, P. Strobel, M. Anne, L.F. Nazar, Electrochemical property: structure relationships in monoclinic $Li_{3-y}V_2(PO_4)_3$, J. Am. Chem. Soc. 125 (2003) 10402–10411.
[41] S.-C. Yin, H. Grondey, P. Strobel, H. Huang, L.F. Nazar, Charge ordering in lithium vanadium phosphates: electrode materials for lithium-ion batteries, J. Am. Chem. Soc. 125 (2003) 326–327.
[42] X.H. Rui, N. Yesibolati, C.H. Chen, $Li_3V_2(PO_4)_3$/C composite as an intercalation-type anode material for lithium-ion batteries, J. Power Sources 196 (2011) 2279–2282.
[43] E. Kobayashi, L.S. Plashnitsa, T. Doi, S. Okada, J. Yamaki, Electrochemical properties of Li symmetric solid-state cell with NASICON-type solid electrolyte and electrodes, Electrochem. Commun. 12 (2010) 894–896.
[44] E. Kobayashi, A. Kitajou, S. Okada, J. Yamaki, Improvement of solid-state symmetric cell performance with lithium vanadium phosphate, J. Power Sources 244 (2013) 312–317.
[45] A. Aboulaich, et al., A new approach to develop safe all-inorganic monolithic Li-ion batteries, Adv. Energy Mater. 1 (2011) 179–183.
[46] G. Delaizir, et al., The stone age revisited: building a monolithic inorganic lithium-ion battery, Adv. Funct. Mater. 22 (2012) 2140–2147.
[47] S. Yu, et al., Monolithic all-phosphate solid-state lithium-ion battery with improved interfacial compatibility, ACS Appl. Mater. Interfaces 10 (2018) 22264–22277.
[48] H. Raj, et al., Stabilizing the NASICON solid electrolyte in an inert atmosphere as a function of physical properties and sintering conditions for solid-state battery fabrication, ACS Appl. Energy Mater. 6 (2023) 1197–1207.
[49] Y. Kee, H. Yun, Reinvestigation of trilithium divanadium(III) tris(orthophosphate), $Li_3V_2(PO_4)_3$, based on single-crystal X-ray data, Acta Crystallogr. Sect. E Struct. Rep. Online 69 (2013) i11–i12.
[50] J. Fouletier, E. Siebert, Accurate monitoring of low oxygen activity in gases with conventional oxygen gauges and pumps, Sci. Technol. zirconia II 618 (1983) 626.
[51] N. Membreño, In Situ Raman study of phase stability of α-$Li_3V_2(PO_4)_3$ upon thermal and laser heating, J. Phys. Chem. C. 117 (2013) 11994–12002.
[52] H. Zhang, Oxygen-loss-induced structural degradation in ε-$LiVOPO_4$, ACS Appl. Mater. Interfaces 15 (2022) 963–972.
[53] H. Zhou, ε-and β-$LiVOPO_4$: phase transformation and electrochemistry, ACS Appl. Mater. Interfaces 9 (2017) 28537–28541.
[54] J.T.S. Irvine, D.C. Sinclair, A.R. West, Electroceramics: characterization by impedance spectroscopy, Adv. Mater. 2 (1990) 132–138.
[55] M. Kleitz, L. Dessemond, M.C. Steil, Model for ion-blocking at internal interfaces in zirconias, Solid State Ion. 75 (1995) 107–115.
[56] S.-C. Yin, P.S. Strobel, H. Grondey, L.F. Nazar, Li2.5V2(PO4)3: a room-temperature analogue to the fast-ion conducting high-temperature γ-phase of Li3V2(PO4)3, Chem. Mater. 16 (2004) 1456–1465.
[57] H. Liu, et al., Kinetics of conventional carbon coated-Li3V2(PO4)3 and nanocomposite Li3V2(PO4)3/graphene as cathode materials for lithium ion batteries, J. Mater. Chem. 22 (2012) 11039.